

INVESTIGATION OF SALT-BEARING SEDIMENTS THROUGH DIGITAL ROCK TECHNOLOGY TOGETHER WITH EXPERIMENTAL CORE ANALYSIS

Marisa B. Rydzy, Ben Anger, Stefan Hertel, Jesse Dietderich, Jorge Patino,
Matthias Appel

Shell International Exploration and Production, Houston, TX

This paper was prepared for presentation at the International Symposium of the Society of Core Analysts held in Vienna, Austria, 27 August – 1 September 2017

ABSTRACT

In this study, we combined digital rock analysis with a variety of experimental core analysis measurements to investigate the effect of salt saturation and distribution on the permeability and porosity of halite-cemented core samples. Medical and micro X-ray CT scans of core sections and 2.54 cm-diameter plugs indicated that the halite generally occurred in form of distinct layers. High-resolution micro X-ray computed tomography (MXCT) images acquired of 0.6 cm-diameter plugs revealed that, on the pore scale, halite appeared to be pore-filling. Pores were either completely filled with halite or did not contain any halite at all. It was also observed that halite preferentially occurred in the larger pores. The porosity and permeability results, both measured and calculated, demonstrated the obstructive effect of halite on storage and flow as well as the decline of both properties with increasing salt saturation. Comparison of calculated and measured values showed that the measured porosity could be up to 6 porosity units (p.u.) higher than the calculated one while the measured permeability of core plugs after salt removal was lower than the calculated one by an order of magnitude. One possible reason for this discrepancy may be the stratified nature of the samples. While the fully salt-saturated plugs appeared homogeneous in MXCT images, post-flood MRI images revealed that the plug was composed of layers with different MRI intensities, i.e. different amounts of water-filled porosity. Consequently, the petrophysical parameters calculated for the mini plugs may only be representative for a section of the core plug. The results of the MRI-assisted core floods emphasized the importance of considering different scales when interpreting and applying the results of digital rocks analysis.

INTRODUCTION

Understanding of how and to what degree an immobile pore fill, such as salt, obstructs the flow of mobile reservoir fluids (water and hydrocarbons), represents an important step in proper reservoir characterization. Basic petrophysical properties, such as porosity

and permeability, are strongly affected by the presence of salt. Mechanical, chemical and, as such, the electrical properties of the formation may be impacted (e.g. Hartman, 1968; Hamilton and Bachman, 1982; Barnabé et al. 1992; Olivarius et al. 2015). **Figure 1** shows X-ray computed images of salt-bearing sandstone on core, plug and pore scale. The images demonstrate the scale dependency of the salt occurrences. They suggest that hydrocarbon storage and flow in these types of sediment will be not only a function of the salt saturation but also a function of the salt distribution. Consequently, interpretation and quantification of key reservoir parameters based on well-logs and other means of geophysical exploration will require validation through digital image analysis at various scales of the salt-bearing sediment in addition traditional core analysis data.

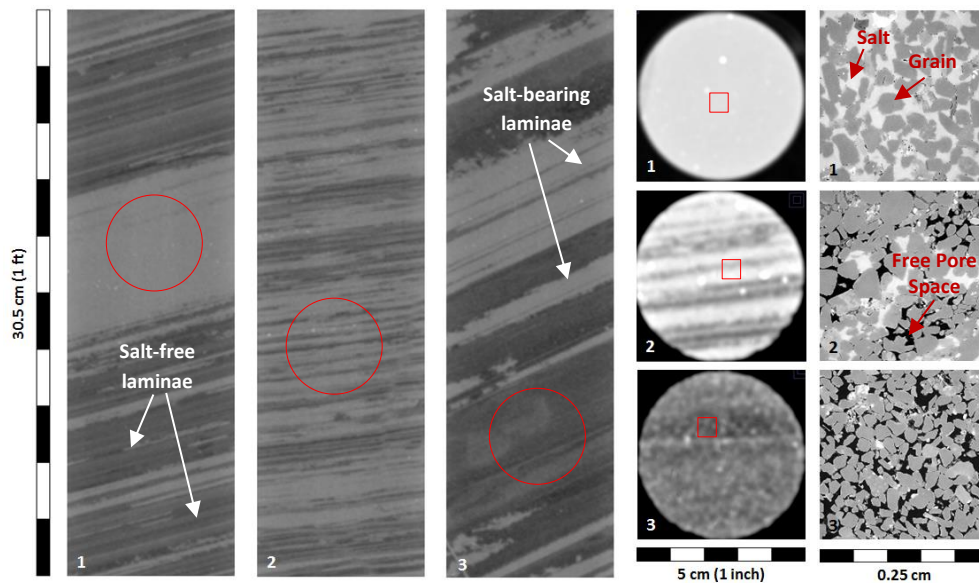


Figure 1: Examples of medical CT scans of 1-ft long core sections and the corresponding 2.54-diameter core plugs that were used in our investigation (Core section CT scans were acquired by CORE LABORATORIES® in Houston, TX). In the MXCT images, black indicates free pore space, grey and light grey/white areas represent sand grains and halite, respectively.

In this paper, we present the findings of our investigation of the porosity and permeability in halite-cemented sandstone. The objective of this study was to characterize the relationship between these key petrophysical parameters with the amount and distribution of the halite. For this purpose, we combined traditional core measurements and core flood (salt dissolution) experiments with imaging techniques, such as macro- and micro-scale X-ray computed tomography (XCT and MXCT, respectively) and magnetic resonance imaging (MRI), as well as qualitative and quantitative image analysis techniques. XCT, MXCT, and MRI have been employed in a variety of geoscience applications (e.g. Sarker and Siddiqui, 2009; Cnudde and Boone, 2013; Thiemeyer et al., 2015), either in the context of quantitative and qualitative analysis of rock structures (e.g. Arns et al. 2005; Wildenschild and Sheppard, 2013) or for monitoring of saturation changes (e.g. Hoffman et al. 1996; Mees et al. 2003; Kneifsey et al. 2007; Erslund et al., 2009). Quantitative analysis of images through “Digital Rocks Technology” (i.e. calculation and simulation

of rock properties based on pore scale images) has emerged in the early 90's. Even though the technology itself can still be considered to be in its infancy, results of recent geoscientific studies that employed digital rocks technology have already demonstrated its potential and value for the petrophysics community (e.g. Arns et al. 2003; Mock et al. 2007).

SAMPLES AND EXPERIMENTAL PROCEDURES

We performed digital image analysis of micro-X-ray CT scans of sixteen 0.6-cm diameter core plugs (“mini plugs”). Porosity measurements and core flood experiments were conducted on regular 2.54-cm diameter core plugs (“macro-plug”).

Eight of the macro-plugs had previously been drilled, trimmed, and cleaned with a mild solvent (cyclohexane) at CORE LABORATORIES[®] in Houston. These plugs were used for the digital rock work. The clean macro-plugs were transferred to our laboratory, where we performed helium porosimetry (**Table 1**) and acquired plug-scale MXCT images of them (**Figure 2**). Afterwards, we drilled a total of sixteen mini plugs out of the macro-plugs. The number of mini plugs per macro-plug are listed in **Table 1**. Their drilling locations are marked in the MXCT images (**Figure 2**). Note, both macro and mini-plugs were drilled without the use of any liquids but with nitrogen gas to preserve the halite.

Table 1: Overview of full-size plugs from which mini plugs were produced

Sample	Description	He- ϕ , %	# Mini Plugs
SLT_001	Fully salt-saturated	6.2	1
SLT_002	Fully salt-saturated	10.2	1
SLT_003	Partially salt-saturated (layers)	12.8	6
SLT_004	Partially salt-saturated (high saturation)	5.3	2
SLT_005	No pore-filling salt	27.0	3
SLT_006	Partially salt-saturated (low saturation)	27.4	2
SLT_007	No pore-filling salt	28.3	3
SLT_008	Fully salt-saturated	-	1

Four sets of additional macro-plugs were drilled, trimmed, and cleaned at our laboratory facility. These plugs were later used in the core flood experiments. The cleaning process involved circulation of toluene for 3-7 days (until the effluent appeared clear) followed by a 12-hour nitrogen purge to dry the samples. During cleaning and drying, the samples were subjected to an effective stress of 3.5 MPa. From monitoring the flow of toluene, we obtained first permeability estimates (**Table 2**). The plug porosity before and after salt-dissolution was estimated by NMR and helium porosimetry, respectively (**Table 2**).

Digital Rock Analysis

MXCT images of the mini plugs were acquired with a ZEISS Xradia 520 Versa scanner. The standard acquisition parameters¹ for each scan yielded 2048x2048x2048 volume of images with a resolution of about 2 μm . The image volumes were reconstructed with

¹ MXCT acquisition parameters: 4X objective, energy of 80 keV/7W and exposure time of 7s yielding an energy count of 7,000, tomography angle = $\pm 180^\circ$ with 6001 projections. Different source filters (LE#2-4) were applied depending of the transmission value.

default settings, exported and processed as raw files. Image processing included reduction of the image stack to a 1024x1024x1024 volume and application of non-local-means filter (Buades et al, 2005). The volume fractions of free and salt-filled pore space were determined from image segmentation (**Figure 3**) performed in IMAGEJ (<https://imagej.nih.gov/ij/>) using manual thresholding based on visual judgement. Pore and grain size distribution were then calculated based on the segmented image volumes using the “porosimetry” method (Wiegmann and Blatt, 2017) within the PORODICT® module of the materials properties simulator GEODICT® (www.math2market.com). Finally, the permeability was calculated for each segmented image volume using an in-house single-phase Lattice-Boltzman flow simulator.

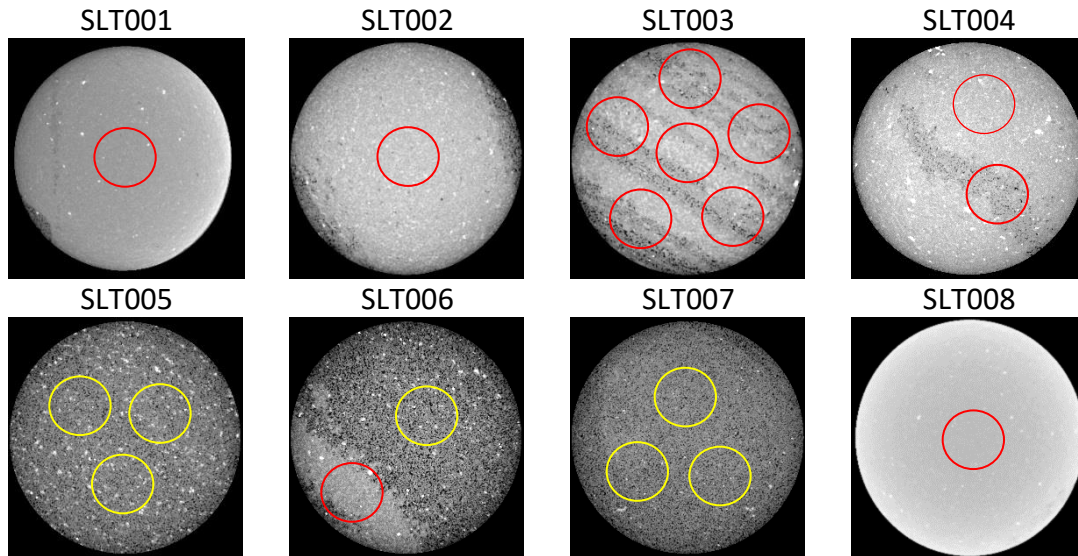


Figure 2: MXCT images of full-size plugs with varying amounts of salt and locations of mini plugs

Table 2: Overview of macro-plugs used in MRI-Flow experiments

Sample	Before salt dissolution					After salt dissolution	
	D, cm	L, cm	NMR- ϕ , %	k_{tol} , md	He- ϕ , %	NMR- ϕ , %	K_{brine} , mD
SLT009-A	2.54	2.51	3.4	4	3.04	23.5	756
SLT010-A	2.55	3.69	3.3	20	4.13	-	669
SLT011-A	2.55	3.72	1.7	25	-	21.1	811

Core Flood Experiments

The core flood experiments were performed in conjunction with magnetic resonance imaging (MRI). The sample was confined inside a sample holder composed of polycarbonate resin (LEXAN™). The sample holder was composed of two halves held together brass screws. Tightening the screws exerted a small confining pressure (less than 10 psi) on the sample. The sample holder was placed inside a vertical bore 2.1T (90.5 MHz for 1H) magnet (ImaCore 3017, MR Solutions and Green Imaging Technologies). The plugs were injected with diluted formation brine (50k ppm equivalent salinity) to initiate salt dissolution. The brine was injected at a constant flow rate (2-5 cc/min) using a Vindum VP-12K pump. Images were acquired at different stages of the core flood

using a Fast Spin Echo (FSE) pulse sequence with three lobe sinc-shaped 90° and 180° pulses of $336 \mu\text{s}$ duration, echo times $TE = 2 \text{ ms}$, 16 signal averages, and eight echoes per RF excitation, leading to acquisition times of 4.3 minutes. The resulting transaxial and/or sagittal 128×128 pixel images provided a field of view of 50 mm and 70 mm, and image resolution of 0.39 mm and 0.55 mm/pixel respectively.

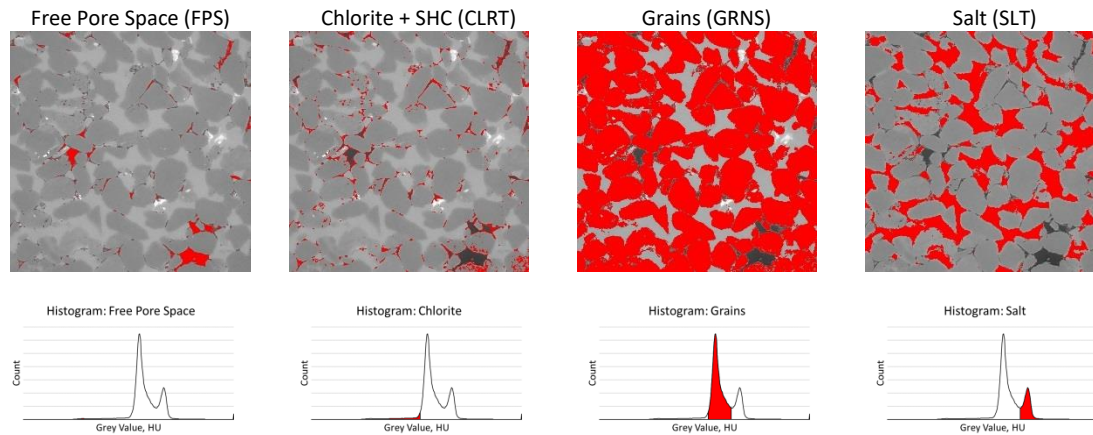


Figure 3: Example of segmentation of MXCT image of mini plugs (SLT006_M1)

RESULTS AND DISCUSSION

Visual inspection of the MXCT images acquired of the mini plugs revealed the principal sediment components that had previously been identified through thin section analysis (M. Jaminski, personal conversation, 2017), namely quartz grains, chlorite overgrowth covered in solid hydrocarbons, and salt (Figure 4).

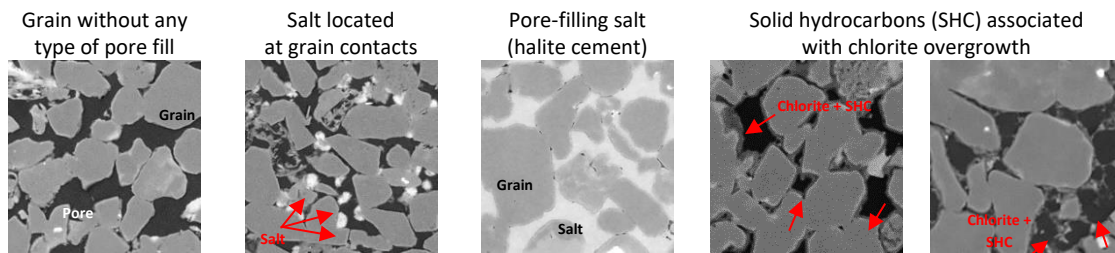


Figure 4: Rock components identified in MXCT images of mini plugs (images shown $1 \times 1 \text{ mm}^2$)

The hydrocarbon-covered chlorite cement was occurred on the grain surfaces as smooth layers that could be several micro-meters thick or in form of thin streaks protruding from the grain surface into the pore space. Salt appeared to occur either as pore-filling halite cement or in form of small polycrystalline agglomerates attached to grain surfaces or located at the grain contacts. At this moment, it remains unclear whether the latter presents a result of cleaning/drying-induced precipitation. In the following, it be treated as part of the rock matrix. The images also revealed that pores were either fully filled with halite or did not contain any salt at all (note, in the following, “partial saturation” will refer to the fraction of salt-filled pore volume compared to the total amount of pore

volume in one mini plug). The salt-filled pores often formed well-defined layers that distinctly stood out in both XCT/ MXCT images of plugs and core sections (**Figures 1 and 2**).

Digital Rock Analysis Results

Based on the calculated salt saturation (S_{salt}), we divided the samples into four groups: 1) fully salt-saturated samples with $S_{\text{salt}} > 97\%$, 2) partially saturated samples with high salt volume ($97\% > S_{\text{salt}} > 85\%$), 3) partially saturated samples with medium to low salt volume ($85\% > S_{\text{salt}}$), and 4) samples without any pore-filling halite. We determined different types of porosity. The “*resolved porosity*” (PHI) only included the free pore space visible in the MXCT images. For samples that did not contain any pore-filling halite, the resolved porosity ranged between 15 and 18%. Up to 3 porosity units (p.u.) of the resolved porosity in these samples could be occupied by the disconnected polycrystalline salt agglomerates mentioned above. In fully salt-saturated samples, the free pore space rarely exceeded 1%. For partially salt-saturated samples, the resolved porosity fell in between. The “*paleo-porosity*” was calculated by adding up free and salt-bearing pore space. For fully and partially salt-saturated samples, we obtained paleo-porosity ranges of 25-33% and 13-33%, respectively. Most samples contained a volume fraction of around 10% of hydrocarbon-covered chlorite cement. Assuming the chlorite contained a *micro-porosity* of 50% (Berger et al. 2009), the additional pore space would increase the overall porosity by around 5 p.u. Measured (**Tables 1 and 2**) and calculated porosity followed similar trends and fell into the same range. The results for individual samples, however, could deviate by up to 6 p.u.

The resolved porosity in the partially halite-saturated samples was generally only partially *percolating*. Especially in samples with higher S_{salt} , the network of connected pores only extended in the directions parallel to bedding. As a result, the *permeability* calculated based on the segmented MXCT images was strongly direction-dependent in the partially halite-saturated samples. Due to the lack of pore-network conductivity, no permeability could be calculated for the fully saturated mini plugs. Instead, a “paleo-permeability” was determined, i.e. the permeability for the host sediment without salt. The paleo permeability reached values in the 1000s of md. In comparison, the permeability calculated for samples without any halite only reached values up to a couple 100 md. **Figure 5** shows the paleo-permeability as a function of salt saturation for the fully salt-saturated samples alongside the calculated actual permeability of the partially saturated and halite-free samples (in the direction of bedding). The plot also includes measured permeabilities for halite-cemented and halite-free macro-plugs.

As expected, the permeability decreases with increasing salt saturation. The permeability decrease loosely follows an exponential trend. However, the results for the partially saturated samples exhibit significant scatter which can be attributed to a) the small number of samples and to b) the dependence of the permeability on the halite distribution (or in this case the orientation of the salt layer to the flow direction). The experimental data showed a less steep increase in permeability from 4-20 mD for fully saturated samples to 600-800 mD for the same samples without the salt.

The elevated paleo-permeabilities obtained for the fully halite-filled samples compared to actual permeabilities determined for the halite-free samples can be attributed to a difference in average *pore size*. Pore sizes (D10, D50, D90) calculated for each mini-plug are shown in **Figure 6**. For the halite-free sediment, pore sizes ranged around 30-60 μm , while the paleo-pore sizes for the fully halite-filled sediment ranged between 40-80 μm . A tendency of halite to occupy larger pore spaces was previously reported in literature. Putnis and Mauthe (2001) observed that halite cement in the Solling Sandstone of the Bunter Formation preferentially occurred in the larger pores. Ott et al. (2014) reported similar observation from laboratory experiments where halite was precipitated through evaporation and CO_2 injection inside a multi-porosity system. Putnis and Mauthe (2001) suggested pore size affected the supersaturation limit for NaCl brine which caused the selective cementation. Similarly, Benavente et al. (2004) cited pore space-induced thermodynamic effects on the brine activity as a factor influencing salt precipitation in porous media. Alternative explanations include prevention of sediment compaction during burial by the halite cement (e.g. Schenk and Schmoker, 1993; Nguyen et al. 2013) and pore-space expansion due to crystallization pressure exerted by the precipitate (e.g. Noiriél et al. 2010).

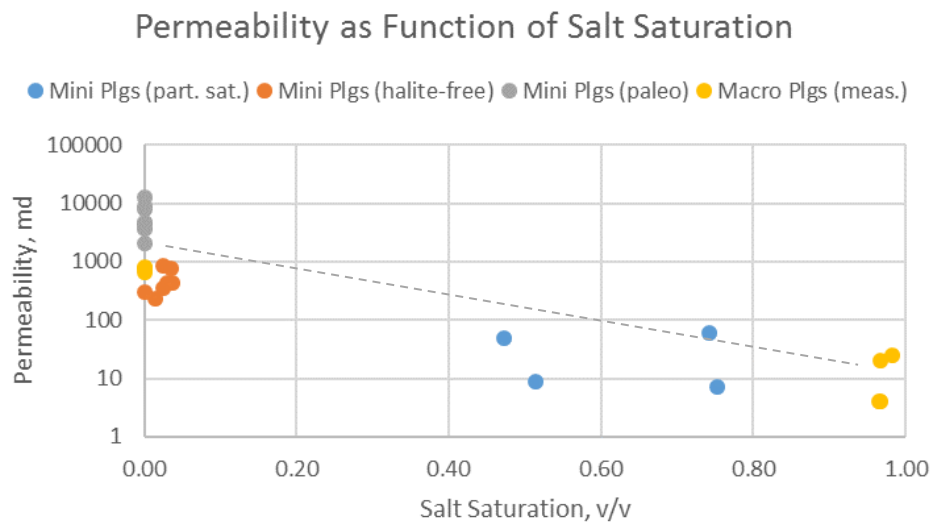


Figure 5: Permeability as function of salt saturation (mini plug permeabilities obtained from simulations)

In this study, the difference in average pore size between fully halite-filled and halite-free sediments can be traced back to a difference in overall *grain size*. This Grain sizes calculated based on the MXCT images of the mini plugs are shown in **Figure 7**. The average grain size for fully halite-filled samples ranged between 10 and 60 μm , while the average grain size for halite-free samples ranged between 5 and 40 μm . Note that the range of grain sizes calculated (10-80 μm) classified the sediment at hand as silty-fine sandstone. Based on the geological analysis of the full core, the sediment was previously classified as fine-medium grained (C. Hern, personal conversation, 2017). The observed

correlation between pore and grain size supports the hypothesis that selective halite precipitation may be influenced by the pore space rather the other way around. Nevertheless, it does not necessarily invalidate alternative explanations, as all the different mechanisms may even act in parallel.

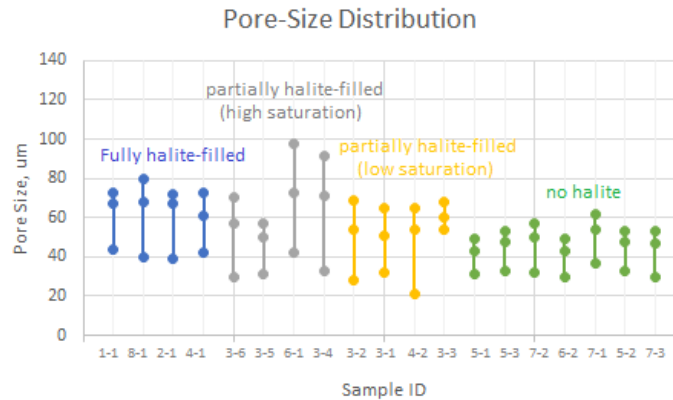


Figure 7: Pore size distribution calculated with PORODICT™ for rock samples with different salt saturations (blue=fully salt-saturated samples, grey=partially salt-saturated (high S_{salt}), yellow= partially salt-saturated (low S_{salt}), green= samples without pore-filling salt, three dots depict D10, D50, and D90)

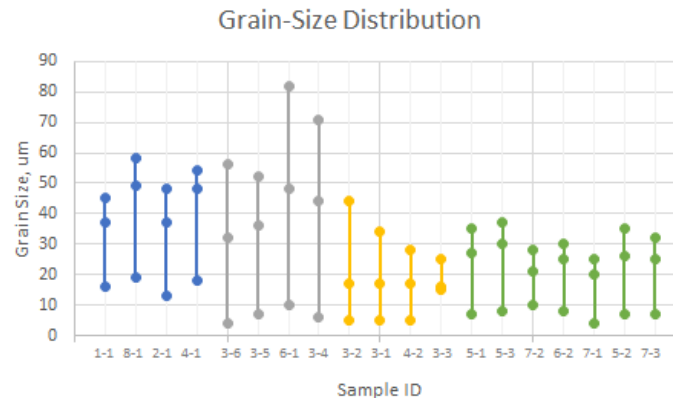


Figure 7: Grain size distribution calculated with PORODICT™ for rock samples with different salt saturations (blue=fully salt-saturated samples, grey=partially salt-saturated (high S_{salt}), yellow= partially salt-saturated (low S_{salt}), green= samples without pore-filling salt, three dots depict D10, D50, and D90)

Salt Dissolution during Core Flooding with Low-Salinity Brine

Figure 7 shows MRI images acquired during the low-salinity water floods of 3 fully halite-cemented macro-cores. MRI measured the nuclear spin density of water within the sample and the water-saturated areas became visible in the MRI scan. The higher water content, the lighter the image appeared. Solid components, such as rock minerals and salt remained undetectable in the MRI. As salt dissolved, more pore space became available for fluid flow and the effective flow cross section increased as can be seen in **Figure 8**. The MRI images that were acquired after salt dissolution had completed show distinct

layers of varying intensity. The different grey values represented different water contents which in turn corresponded to different porosities and potentially different pore sizes. Due to the heterogeneity of the macro-plugs, the porosities and permeabilities of the extracted mini plugs may not have been representative of the whole plug but merely of one layer or two. Consequently, even in fully salt-saturated samples that appear homogeneous in XCT or MXCT images, multiple mini plugs should be extracted for digital rock analysis. Interestingly though, the salt dissolution front did not appear to be impacted by the stratified makeup of the sample as it was observed to cut across layers (Figure 7).

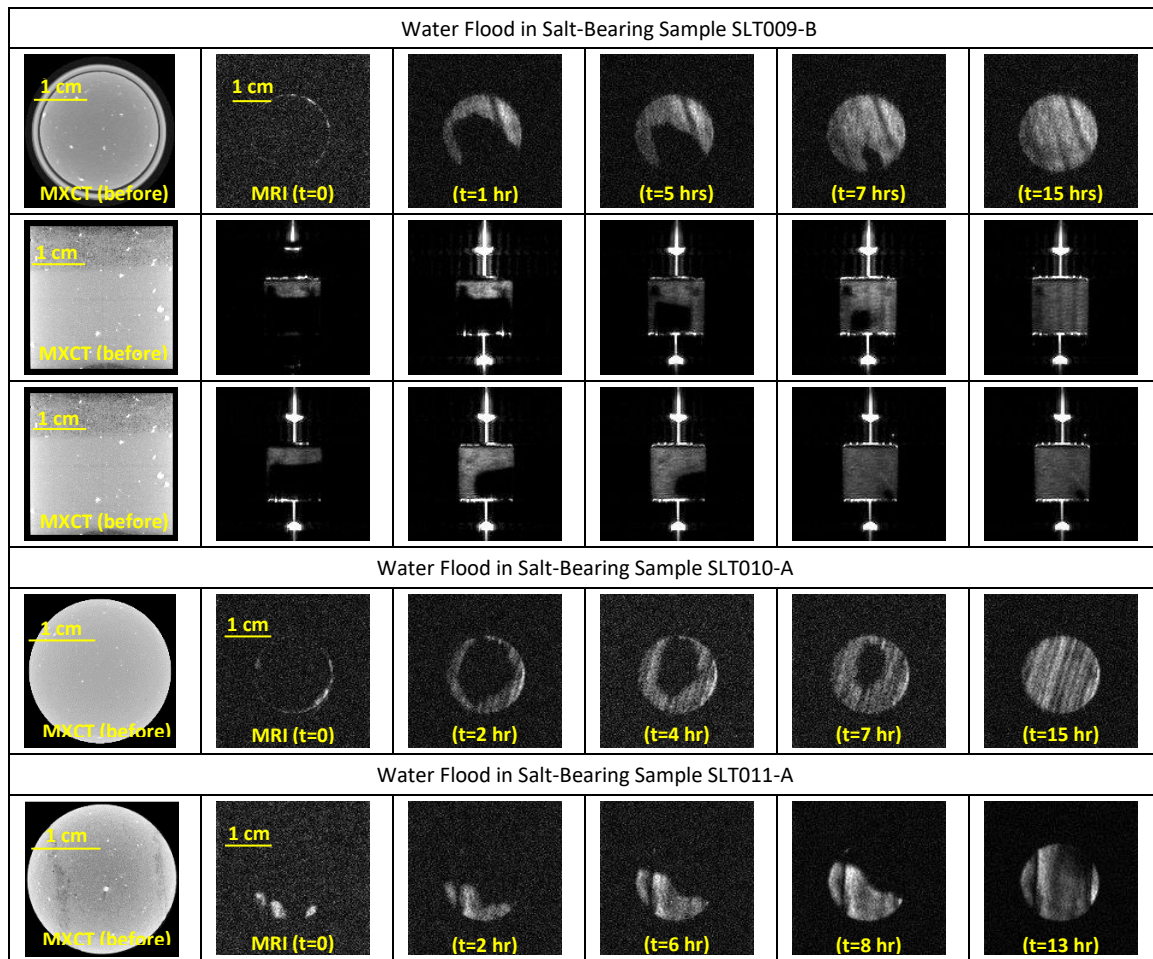


Figure 8: MXCT and MRI images acquired of Samples SLT010-A, SLT011-A, and SLT009-B before, during, and after the water flood experiment. All three planes (coronal, sagittal, and transaxial) were only recorded for the last sample. The duration of the salt dissolution process rarely exceeded 24 hours.

CONCLUSIONS

The combination of core analysis measurements, MRI, and digital rock analysis was shown to be a valuable approach in the investigation of halite-cemented sandstones. The qualitative and quantitative results of the analysis of pore scale images provided useful

insights into the interplay between halite cementation. It was shown that the halite cement occurred primarily in the larger pore spaces which generally arose from larger grain sizes, and that permeability and porosity declined drastically with higher halite content. Furthermore, the MXCT images showed a bimodal halite distribution occurring as layers in the XCT images with either fully cemented pore space or free pore space. While a full quantitative evaluation of the MRI images is still outstanding, it could be shown that the salt masked the stratified makeup of the plugs and that unconformities in the distribution of the halite cement determined that starting point and propagation of the salt dissolution front. As a next step in the investigation of halite-cemented sediments, we will attempt to utilize the combination of core flood, permeability measurements and imaging to better quantify the relationship between salt saturation, its distribution across the core plug, and permeability.

ACKNOWLEDGEMENTS

We would like to thank Keith Love, Matthew Knuth, David Janson, and Menno Hartemink for providing the samples and funding for this study. Many thanks to Gary Moore, Steve Ellis, Thomas Kubicek, Sharon Patterson, Dmitry Shaporov, Jorge Patino, Vivian Morah, and Kirk Smith for their assistance with core handling, sample preparation, and measurements. Mazina Jaminski and Carolyn Hern supported our efforts through fruitful discussions about the geological and petrological background of the sediments investigated. As for the digital rock analysis, the non-local means filter and single-phase Lattice-Boltzman Simulator were developed and provided by Alon Arad and Omar Alpak, respectively.

REFERENCES

- Ajayendra, 'AJ'Kumar, Z. G.,L. Morales, T. Griffin, and J. Dacy. (2016), Micro-CT Imaging—A Powerful Tool for Screening and Rapid Quantification of Rock Properties, EG Technical Program Expanded Abstracts, 1477-1480
- Arns, C.H., A. Sakellariou, T.J. Senden, A.P. Sheppard, R.M. Sok, M.A. Knackstedt, W. V. Pinczewski, and G.F. Bunn (2003) Virtual core laboratory: Properties of reservoir rock derived from X-ray CT images,
- Benavente, D., M.A. Garcia del Cura, J. Garcia-Guinea, S. Sanchez-Moral, and S. Ordonez (2004), Role of pore structure in salt crystallization in unsaturated porous stone, *Journal of Crystal Growth* 260, 532-544
- Berger A., S. Gier and P. Krois (2009) Porosity-preserving chlorite cements in shallow-marine volcanoclastic sandstones: Evidence from Cretaceous sandstones of the Sawan gas field, Pakistan. *AAPG Bulletin* 93(5), 595–615
- Bernabé, Y., Fryer, D. T., & Hayes, J. A. (1992). The effect of cement on the strength of granular rocks. *Geophysical Research Letters*, 19(14), 1511-1514.

Buades, A., B. Coll, and J.M. Morel (2005), A non-local algorithm for image denoising, in *Computer Vision and Pattern Recognition, 2005*, IEEE Computer Society Conference Vol. 2, 60-65

Cnudde, V., and M.N. Boone, High-Resolution X-ray computed tomography in geosciences: A review of the current technology and applications, *Earth Science Reviews* 123, 1-17

Ersland, G., J. Husebø, A. Graue, and B. Kvamme (2009). Transport and storage of CO₂ in natural gas hydrate reservoirs, *Energy Procedia* 1(1), 3477-3484

Fredrich, J. T., Lakshtanov, D. L., Lane, N. M., Liu, E. B., Natarajan, C. S., Ni, D. M., & Toms, J. J. (2014, October). Digital rocks: developing an emerging technology through to a proven capability deployed in the business. In *SPE Annual Technical Conference and Exhibition*. Society of Petroleum Engineers.

Gevantman, L.H., Lorenz, J., Haas, J.L. Jr., Clynne, M.A., & Potter, R.W. II. (1981). Physical properties data for rock salt. United States.

Hamilton, E. L., & Bachman, R. T. (1982). Sound velocity and related properties of marine sediments. *The Journal of the Acoustical Society of America*, 72(6), 1891-1904.

Hoffman, F., D. Ronen, and Z. Pearl (1996). Evaluation of flow characteristics of a sand column using magnetic resonance imaging, *Journal of Contaminant Hydrology*, 22(1-2), 95-107.

Kneafsey, T. J., L. Tomutsa, G.J. Moridis, Y. Seol, B.M. Freifeld, C.E. Taylor, and A. Gupta (2007), Methane hydrate formation and dissociation in a partially saturated core-scale sand sample, *Journal of Petroleum Science and Engineering* 56(1), 108-126.

Laier, T., & Nielsen, B. L. (1989). Cementing halite in Triassic Bunter Sandstone (Tønder, southwest Denmark) as a result of hyperfiltration of brines. *Chemical Geology*, 76(3-4), 353-363.

Mees, F., R. Swennen, M. Van Geet, and P. Jacobs (2003), Applications of X-ray computed tomography in the geosciences, *Geological Society Special Publications* 215, 243-249.

Nguyen, B.T., S.J. Jones, N.R. Goult, A.J. Middleton, N. Grant, A. Ferguson, and L. Bowen (2013), The role of fluid pressure and diagenetic cements for porosity preservation in Triassic fluvial reservoirs of the Central Graben, North Sea, *AAPG bulletin* 97(8), 1273-1302.

Noiriel, C., F. Renard, M.L. Doan, and J.P. Gratier (2010), Intense fracturing and fracture sealing induced by mineral growth in porous rocks, *Chemical Geology*, 269(3), 197-209.

Olivarius, M., Weibel, R., Hjuler, M. L., Kristensen, L., Mathiesen, A., Nielsen, L. H., & Kjølner, C. (2015). Diagenetic effects on porosity–permeability relationships in red beds of the Lower Triassic Bunter Sandstone Formation in the North German Basin. *Sedimentary Geology*, 321, 139-153.

Ott, H., M. Andrew, J. Snippe, and M.J. Blunt (2014), Microscale solute transport and precipitation in complex rock during drying, *Geophysical Research Letters* 41, 8369-8376
Putnis, A. and G. Mauthe (2001), The effect of pore size on cementation in porous rocks, *Geofluids* 1, 37-41.

Sarker, M.R.H., and S. Siddiqui (2009), Advances in Micro-CT Based Evaluation of Reservoir Rocks, SPE 126039, presented at the 2009 Saudi Arabia Section Technical Symposium and Exhibition, AlKhobar, Saudi Arabia, May 9-11.

Schenk, C.J. and J.W. Schmoker (1993), Role of Halite in the Evolution of Sandstone Porosity, Upper Jurassic Norphlet Formation, Mississippi Salt Basin, Gulf Coast Association of Geological Societies Transactions 43, 357-362.

Thiemeyer, N., J. Habersetzer, Mark Peinl, Gernold Zulauf, and J. Hammer (2015), The application of high resolution X-ray computed tomography on naturally deformed rock salt: Multi-scale investigation of the structural inventory, *Journal of Structural Geology* 77, 92-106.

Wiegmann, A. and E. Glatt (2017), Porodict, GeoDict 2017 User Guide, math2market